International Journal of Mechanical Sciences 110 (2016) 190–200

Contents lists available at ScienceDirect

International Journal of Mechanical Sciences

journal homepage: www.elsevier.com/locate/ijmecsci

Creep strain measurement using a potential drop technique

Joseph Corcoran [a,*], Paul Hooper [a], Catrin Davies [a], Peter B. Nagy [a,b], Peter Cawley [a]

[a] Department of Mechanical Engineering, Imperial College London, London SW7 2AZ, UK
[b] Department of Aerospace Engineering and Engineering Mechanics, University of Cincinnati, OH 45221-0070, USA

ARTICLE INFO

Article history:
Received 19 February 2016
Received in revised form
11 March 2016
Accepted 16 March 2016
Available online 21 March 2016

Keywords:
ACPD
DCPD
Potential drop
Creep
Strain

ABSTRACT

This paper will demonstrate the use of a potential drop sensor to monitor strain. In particular, the suitability of the technique to high temperature or harsh environment applications presents an opportunity for monitoring strain in components operating under creep conditions. Monitoring creep damage in power station components is a long standing technological challenge to the non-destructive evaluation community. It is well established in the literature that strain rate serves as an excellent indicator of the progress of creep damage and can be used for remnant life calculations. To facilitate the use of such strain rate based evaluation methods, a permanently installed, strain sensitive, potential drop technique has been developed. The technique has very simple and robust hardware lending itself to use at high temperatures or in harsh environments. Strain inversions are presented and demonstrated experimentally; a room temperature, plastic deformation experiment is used for validation and additionally an accelerated creep test demonstrates operation at high temperature (600 °C+). Excellent agreement is shown between potential drop inverted strain and control measurements.

1. Introduction

Creep is frequently the life limiting mechanism of high-temperature, high-pressure power station components such as steam headers or pipe work [1–3]. Non-destructive evaluation of creep damage stands as a particularly difficult problem due to a) the range of mechanisms which constitute creep damage [4], b) the close proximity to failure where damage mechanisms may become evident [5] and c) the lack of selectivity of a given sensor to a particular damage mechanism [6]. The strain, or more specifically the strain rate, of a component is well known to provide valuable information on creep integrity and has been suggested for use in remnant life estimate calculations [4,7,8].

In a laboratory environment strain monitoring is the standard means of evaluating the creep state of the component under test [3,9,10]. A technique for strain monitoring power station components has been a long standing technological challenge [11–13]. A range of off-load dimensional measurements have been adopted in the past but even when aided by specially designed features, such as 'creep pips', the repeatability of measurements has been unsatisfactory [11,14]. Additionally, the inherent infrequency of data collection undermines the possibility of accurate strain rate estimates.

The on-load measurement technique that has held the most promise has been the capacitance gauge. Capacitance gauges have been available since the 1970s [15–17] and come in a range of designs [18]. SJB Engineering UK, who have provided gauges for Eskom [19] and previously PowerGen [13], report a number of issues with the gauges which will be inherent in any sensor which is to be mounted to the surface of a component and uses a transduction device above the surface. Notably oxide growth under the sensor or weld relaxation can cause rocking and mechanical instability and measuring strain on a curved surface (for example in the circumferential direction in straight pipes and the doubly curved geometry of pipe bends) will require special calibration. Technological limitations such as reliability in harsh environments and long term drift, when combined with economic and practical difficulties of being delicate, difficult to install and expensive [11] are believed to be key factors in the lack of widespread adoption.

Potential drop measurements are commonly used to inspect or monitor crack growth in the laboratory and commercial systems are available for use in industrial settings [20–22]. The effective conductivity of damaged materials may decrease as a result of microstructural or macroscopic impediments to current flow associated with creep damage and so potential drop measurements have been suggested as promising in the past [6]. With the exception of macroscopic cracking associated with localised damage accumulation [23] and the influence of thermal exposure

* Corresponding author.
E-mail address: joseph.corcoran07@imperial.ac.uk (J. Corcoran).

http://dx.doi.org/10.1016/j.ijmecsci.2016.03.015

on solute depletion [24–27] there is little convincing use of potential drop measurements to monitor creep damage through conductivity changes. On the other hand, by permanently attaching electrodes to the surface of the component potential drop measurements also become sensitive to strain; as the component deforms the electrodes move relative to each other. The most convincing previously reported realisation of this as a useful tool comes from the work of Vasatis and Pelloux in a series of works in the 1980s [28–30]. Direct Current Potential Drop (DCPD) measurements were taken on narrow cylindrical uniaxial specimens and strain measurements were successfully inverted from the resistance measurements.

A permanently installed, four point, potential drop strain sensor has been developed that has extremely simple and robust hardware at component level. The use of a quasi-DC inspection current provides enhanced noise performance [31,32] whilst suppressing the skin effect [31,33,34] that would otherwise undermine measurements in the ferromagnetic materials of interest to the electricity generation industry; the enhanced noise performance enables low-power operation lending the technique to remote, continuous monitoring. The realisation of a permanently installed sensor capable of frequent readings will enable the strain rate measurements of interest for creep integrity assessment of power station components.

This paper gives the background to the proposed permanently installed, low-frequency, potential drop strain measurement and provide analytical relationships between strain and resistance. Two inversion options are presented with discussion on the selection and attributes of each. The technique and inversions are then demonstrated using two experiments, a room temperature tensile test component which allows detailed independent measurements and additionally a uniaxially loaded accelerated creep test component to show high-temperature capability. Further consideration is given to utilisation in the power station context where creep is known to be a major life limiting damage mechanism.

2. Low-frequency, square configuration potential drop measurements

A brief description of the proposed technique is given here; more detail can be found in prior work by Madhi and Nagy [33]. Four electrodes, in the form of stainless steel pins, are spot welded in a square configuration to the surface of a component. Electrodes forming one side of the square are used for injecting a known current, I, while electrodes forming the opposite side are used for measuring the resulting potential difference ΔV as illustrated in Fig. 1. The transfer resistance is calculated as $R=\Delta V/I$ (as at quasi-DC frequencies the reactive component should be insignificant). Following this, a second measurement is taken using the remaining sides resulting in an 'orthogonal' resistance reading.

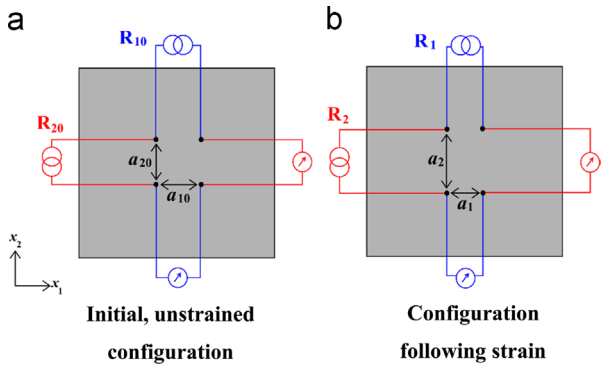

Fig. 1. Schematic showing potential drop measurement arrangement. (a) The initial, unstrained configuratione and (b) the influence of component strain on electrode position and resistance measurement.

Alternating currents are subject to the skin-effect, the current being electromagnetically constricted to the surface of the component, resulting in an exponentially decreasing current density with depth. The skin-depth, δ, the depth at which the current density is $1/e$ (~37%) of the surface density, is described by the equation,

$$\delta=\frac{1}{\sqrt{\sigma\pi f\mu}} \tag{1}$$

where σ is the electrical conductivity, f is the current frequency and μ is the magnetic permeability of the component. In the ferromagnetic materials of interest to the power industry the magnetic permeability is a function of many different parameters including temperature, stress, thermal history, cold work and alloy composition [35]; it is therefore expected to change significantly during operation, consequently influencing the skin-depth and the measured resistance. If the inspection frequency is lowered and the skin depth increased, then the current penetration will eventually be limited instead by the smaller of the electrode separation or the component thickness and no longer influenced by spurious changes in permeability. It is important that the electrode separation is smaller than the component thickness to remove dependence on the proximity of the back wall that could otherwise be influenced by non-strain related thickness loss, for example oxidation.

While it is important to use a sufficiently low inspection frequency to suppress the influence of the skin effect it is also beneficial to use as high a frequency as possible to improve the noise performance. The use of alternating currents permits the use of phase locked detection and the separation of the signal from DC sources such as thermoelectric effects. Random 'flicker' noise power increases at lower frequencies with $1/f$ distribution and it is therefore beneficial to use as high a frequency as possible to reduce the noise density [32]; in this paper inspection frequencies of 1–2 Hz are used. The noise performance permits use of inspection currents much lower than the DC alternative; typically around 100 mA as opposed to tens or hundreds of Amps [20,22,36]. More information on the instrumentation and implementation can be found in [31].

Conventionally, potential drop measurements are implemented using an 'in-line' electrode configuration [20]. In this instance a square electrode configuration is adopted to a) reduce the number of electrodes when taking orthogonal measurements and b) to enhance strain sensitivity [31].

Madhi and Nagy provide an analytical description of the potential distribution produced by a DC current source in an anisotropic half-space [33].

$$\varphi=\frac{I\sqrt{\rho_1\rho_2\rho_3}}{2\pi}\left(\frac{1}{\sqrt{\rho_1(x_1-s_1)^2+\rho_2(x_2-s_2)^2+\rho_3(x_3-s_3)^2}}\right)+\varphi_0 \tag{2}$$

where φ is the electric potential at a given field point of spatial coordinates (x_1,x_2,x_3) from a point current source injecting current I with coordinates (s_1,s_2,s_3). The component will have resistivity components (ρ_1,ρ_2,ρ_3) in the three spatial coordinates. φ_0 is an integration constant that corresponds to the electric potential at some remote point which will cancel out when measuring a potential difference.

Assuming the source and field point both lie on the free surface of the principal plane ($x_3=0$) and the electrodes are aligned in the x_1 and x_2 directions then the transfer resistances in these two orthogonal directions can be found using superposition [33]. Following the notation used in Fig. 1 the two orthogonal resistances

are given by,

$$R_1 = \frac{\sqrt{\rho_1\rho_2\rho_3}}{\pi}\left(\frac{1}{\sqrt{\rho_2 a_2^2}} - \frac{1}{\sqrt{\rho_1 a_1^2 + \rho_2 a_2^2}}\right)$$
$$R_2 = \frac{\sqrt{\rho_1\rho_2\rho_3}}{\pi}\left(\frac{1}{\sqrt{\rho_1 a_1^2}} - \frac{1}{\sqrt{\rho_1 a_1^2 + \rho_2 a_2^2}}\right) \quad (3)$$

where a is the electrode separation and ρ is the electrical resistivity in the orthogonal spatial directions denoted by the subscripts 1 and 2. Assuming isotropic resistivity,

$$R_1 = \frac{\rho}{\pi}\left(\frac{1}{a_2} - \frac{1}{\sqrt{a_1^2 + a_2^2}}\right)$$
$$R_2 = \frac{\rho}{\pi}\left(\frac{1}{a_1} - \frac{1}{\sqrt{a_1^2 + a_2^2}}\right). \quad (4)$$

a_1 and a_2 can be written in terms of their initial length a_{10} and a_{20} and the orthogonal engineering strains ε_1 and ε_2 in the x_1 and x_2 directions respectively: $a_1 = a_{10}(1+\varepsilon_1)$ and $a_2 = a_{20}(1+\varepsilon_2)$. At this point it will be assumed that the initial electrode geometry is square, $a_0 \approx a_{10} \approx a_{20}$ for simplicity, but means of accounting for imperfect electrode placement will be addressed later. Substituting for a_1 and a_2 yields,

$$R_1 = \frac{\rho}{\pi a_0}\left(\frac{1}{(1+\varepsilon_2)} - \frac{1}{\sqrt{(1+\varepsilon_1)^2 + (1+\varepsilon_2)^2}}\right)$$
$$R_2 = \frac{\rho}{\pi a_0}\left(\frac{1}{(1+\varepsilon_1)} - \frac{1}{\sqrt{(1+\varepsilon_1)^2 + (1+\varepsilon_2)^2}}\right) \quad (5)$$

It is also convenient to normalise the resistances to their initial values as the initial resistivity or geometry is usually of little interest; it is the change of state that provides the information. The initial resistances are:

$$R_{10} = R_{20} = \frac{\rho_0}{\pi a_0}\left(1 - \frac{1}{\sqrt{2}}\right) \quad (6)$$

The inverse of $1 - 1/\sqrt{2}$ is a value that will be frequently used and so will be assigned the symbol, $s \approx 3.41$.

$$\frac{R_1}{R_{10}} = s\frac{\rho}{\rho_o}\left(\frac{1}{(1+\varepsilon_2)} - \frac{1}{\sqrt{(1+\varepsilon_1)^2 + (1+\varepsilon_2)^2}}\right)$$
$$\frac{R_2}{R_{20}} = s\frac{\rho}{\rho_o}\left(\frac{1}{(1+\varepsilon_1)} - \frac{1}{\sqrt{(1+\varepsilon_1)^2 + (1+\varepsilon_2)^2}}\right) \quad (7)$$

It is Eq. (7) that will be used for strain inversion. Evidently, the sensitivity of the resistance measurements to resistivity presents a challenge. The electrical resistivity is strongly dependent on reversible temperature effects and, to a much lesser extent, may also be influenced by long term microstructural evolution. Resistivity change must therefore be addressed in any successful inversion procedure.

2.1. Normalised Resistance Ratio inversion

Isotropic resistivity change can be easily and effectively suppressed by taking the ratio of the two orthogonal measurements, thereby cancelling the resistivity terms [33]. Additionally, the ratio of the orthogonal measurements will have the equivalent effect of suppressing instrument gain drift not explicitly included here. The Normalised Resistance Ratio, *NRR*, is given by,

$$NRR = \frac{R_1}{R_{10}} \Big/ \frac{R_2}{R_{20}} = \frac{\frac{1}{(1+\varepsilon_2)} - \frac{1}{\sqrt{(1+\varepsilon_1)^2 + (1+\varepsilon_2)^2}}}{\frac{1}{(1+\varepsilon_1)} - \frac{1}{\sqrt{(1+\varepsilon_1)^2 + (1+\varepsilon_2)^2}}} \quad (8)$$

Madhi and Nagy [33] shown that Eq. (8) can be approximated using a power approximation,

$$NRR = \left(\frac{\frac{a_1}{a_{10}}}{\frac{a_2}{a_{20}}}\right)^s = \left(\frac{1+\varepsilon_1}{1+\varepsilon_2}\right)^s \quad (9)$$

It is therefore evident that the use of the resistance ratio compromises the quality of information, preserving only information on the aspect ratio. In creep and plasticity the deformation of a component is governed by shear and therefore the distribution of strain is dictated by the deviatoric stress tensor [37]. Therefore, in order to relate orthogonal strain components, the stress state must be known. In the case of uniaxial loading in the x_1 direction this is trivial as $\varepsilon_2 = -0.5\varepsilon_1$.

$$NRR = \left(\frac{1+\varepsilon_{1uniaxial}}{1-0.5\varepsilon_{1uniaixal}}\right)^s \quad (10)$$

or,

$$\varepsilon_{1uniaxial} = \frac{NRR^{1/s} - 1}{0.5\,NRR^{1/s} + 1}, \quad (11)$$

allowing the strain in uniaxial stress conditions to be obtained. Unfortunately however, the stress state at a given position on a power station component is unlikely to be known adequately. Therefore an alternative approach is required for situations with an unknown stress state.

2.2. Normalised Resistance inversion

In cases where the stress state is not well defined then ε_1 and ε_2 must be treated as independent (note that as there is no sensitivity to ε_3 they cannot be coupled through conservation of volume). It is not possible to obtain a resistivity independent inversion to recover both strain components. A resistivity coupled Normalised Resistance inversion is possible on this basis by combining Eqs. (7) and (9) yielding,

$$\frac{1+\varepsilon_1}{\rho/\rho_0} = s\frac{NRR^{1/s} - 1}{\frac{R_1}{R_{10}} - \frac{R_2}{R_{20}}}$$
$$\frac{1+\varepsilon_2}{\rho/\rho_0} = s\frac{\left(\frac{1}{NRR}\right)^{1/s} - 1}{\frac{R_2}{R_{20}} - \frac{R_1}{R_{10}}} \quad (12)$$

In order to make use of this inversion it is necessary to address the resistivity dependence of Eq. (12). In certain situations, such as constant temperature, short duration accelerated creep tests, the resistivity may be sufficiently stable for its variation to be neglected. Under power station conditions however it must be assessed and compensated for. The *estimated* resistivity change will be denoted as r/r_0 allowing for the Normalised Resistance strain inversion,

$$\varepsilon_1 = \frac{r}{r_0}s\frac{NRR^{1/s} - 1}{\frac{R_1}{R_{10}} - \frac{R_2}{R_{20}}} - 1$$
$$\varepsilon_2 = \frac{r}{r_0}s\frac{NRR^{-1/s} - 1}{\frac{R_2}{R_{20}} - \frac{R_1}{R_{10}}} - 1 \quad (13)$$

Imperfect resistivity compensation will provide a source of error in the inversion of resistance data. Another equivalent effect results from the measurement system where gain drift or instability would have a similar scaling effect as resistivity change.

The authors do not believe it is possible to combine further, for example in-line potential drop measurements, to provide a

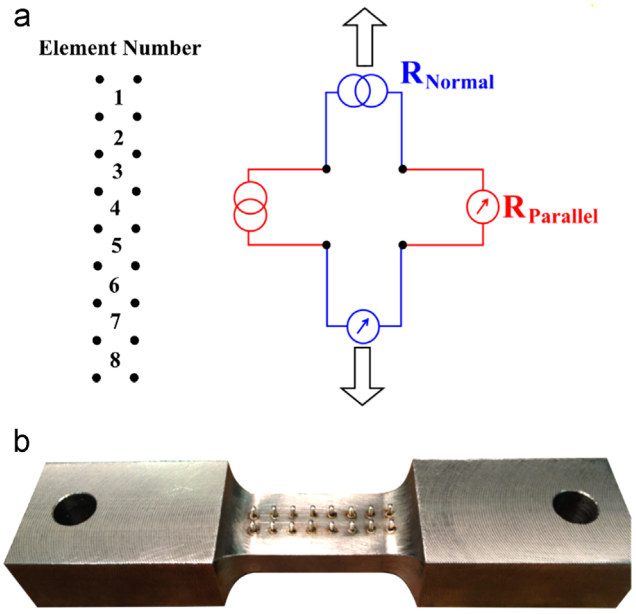

Fig. 2. (a) Schematic showing potential drop array measurement arrangement. (b) Photograph of a high temperature creep specimen with an array of 5 mm electrode separation potential drop sensors along one face.

significantly independent equation that will allow cancelling of the resistivity terms. Though it is worth mentioning that it may be possible by combining 'thin' measurements (where the electrode separation is much larger than the component thickness) although these will be sensitive to non-strain related thickness changes.

2.3. Potential drop array measurements

The proposed square arrangement potential drop technique can also be implemented in an array formation providing full coverage of the component length and may reveal significant local strain variation, as demonstrated in the experimental results of this paper.

The structure of a 1×8 element array is shown in Fig. 2(a). Each element of the array is configured to measure the two orthogonal resistances, resulting in 16 resistance measurements for the full array. A photograph of a potential drop array installed on a uniaxial creep component is shown in Fig. 2(b); 1.5 mm stainless steel pins with separation of 5 mm are shown.

3. Small component considerations

In order to successfully invert resistance to strain it is necessary to assume all resistance change is due to the geometric effect of electrode migration. Unfortunately, on the narrow test components common to laboratory testing the proximity of the component edges restricts the current flow and distorts the resulting potential field; the measured potential difference is increased as a result of the so called 'edge effect'. Moreover, as the component and electrode configuration deforms with strain, the effective proximity to the edges changes and so too must the edge effect. It is necessary to compensate for this effect in the small geometry components that the inversions will be demonstrated on.

3.1. Edge effects

Lu et al. offer an analytical solution for the edge effects in a four-point DC potential drop measurement that is directly applicable to this quasi-DC case [38]. A square arrangement potential drop measurement can be modelled on a component that is infinite in one surface direction, but finite both in the normal direction and through the thickness, replicating a slender tensile test component. In Fig. 3 the resistances from the finite geometry slender component are normalised to the resistance that would result from an infinite component of equal electrical conductivity. The two orthogonal resistances are shown separately in Fig. 3(a) and (b). Both component thickness and width are normalised to the square electrode separation.

The solution can then be adapted so that the effect of strain accumulation is imposed on the model. Component and electrode configuration dimensions are extended in the infinite (loading) direction and contracted in the orthogonal, finite dimensions; uniaxial loading is assumed as indicated in the schematic of Fig. 4. Resistances are then calculated for the new deformed configuration and the increase in resistance from the unstrained values can then be equated to strain using the inversions.

The error between the inverted strain calculated from a component with edge effects and the strain imposed increases linearly with deformation. Due to the linearity of the error, in order to compensate for the edge effects in the strain inversions a simple dividing factor can be applied to calculated strain values, so that $\varepsilon_{corrected} \approx \varepsilon_{calculated}/k$, where $\varepsilon_{calculated}$ is the strain calculated from the inversion of potential drop data, k is the correction factor and $\varepsilon_{corrected}$ is the improved approximation of the real strain value. The correction factor is calculated from dividing the strain calculated from the solutions derived from Lu et al. by the strain imposed on the solution. The correction factors are a function of the initial geometry of the component; correction factors are given in Fig. 5 for a) the Normalised Resistance inversion for the strain calculated in the long component axis, usually in the loading direction, b) the Normalised Resistance inversion for the strain calculated in the short component axis and c) the Normalised Resistance Ratio inversion.

From Fig. 5 it can be seen that the Normalised Resistance inversion is much more sensitive to edge effects than the Normalised Resistance Ratio inversion. With reference to Fig. 3, with a normalised width greater than ~4 then the influence of the edges on both orthogonal resistances is similar and therefore by taking the ratio much of the effect is cancelled. The use of the Normalised Resistance Ratio inversion is therefore strongly encouraged over the use of the Normalised Resistance inversion in components where edge effects are significant.

Clearly from Fig. 4 compensation of results from components with a normalised width of less than two or a normalised thickness of less than one should not be attempted. Further, a width of >5 times electrode separation and a thickness of >2 times electrode separation is desirable in order for correction to be successful; a practical lower limit for electrode separation is from experience around 4–5 mm.

It is worth noting that strain inversions for thin components are equally possible, in which case correction factors will have to be applied to account for thicker components, this case is not included here as non-strain related thickness changes that are likely to occur under creep conditions will be difficult to account for.

3.2. Imperfect electrode placement

Implicit in the derivation of Eq. (5) and subsequent equations is the assumption that the initial geometry is square. In practice this will be violated to some degree; the random or systematic extent of electrode placement uncertainty will depend on the electrode attachment process. In large power station or laboratory test components where the edge effects are negligible, the influence of imperfect electrode positioning can be addressed. Using Eq. (9) the initial effective aspect ratio, $\gamma_0 = a_{10}/a_{20}$, can be estimated; the relationship $a_{10} \approx \gamma_0 a_{20}$ can then be substituted into Eq. (4). The

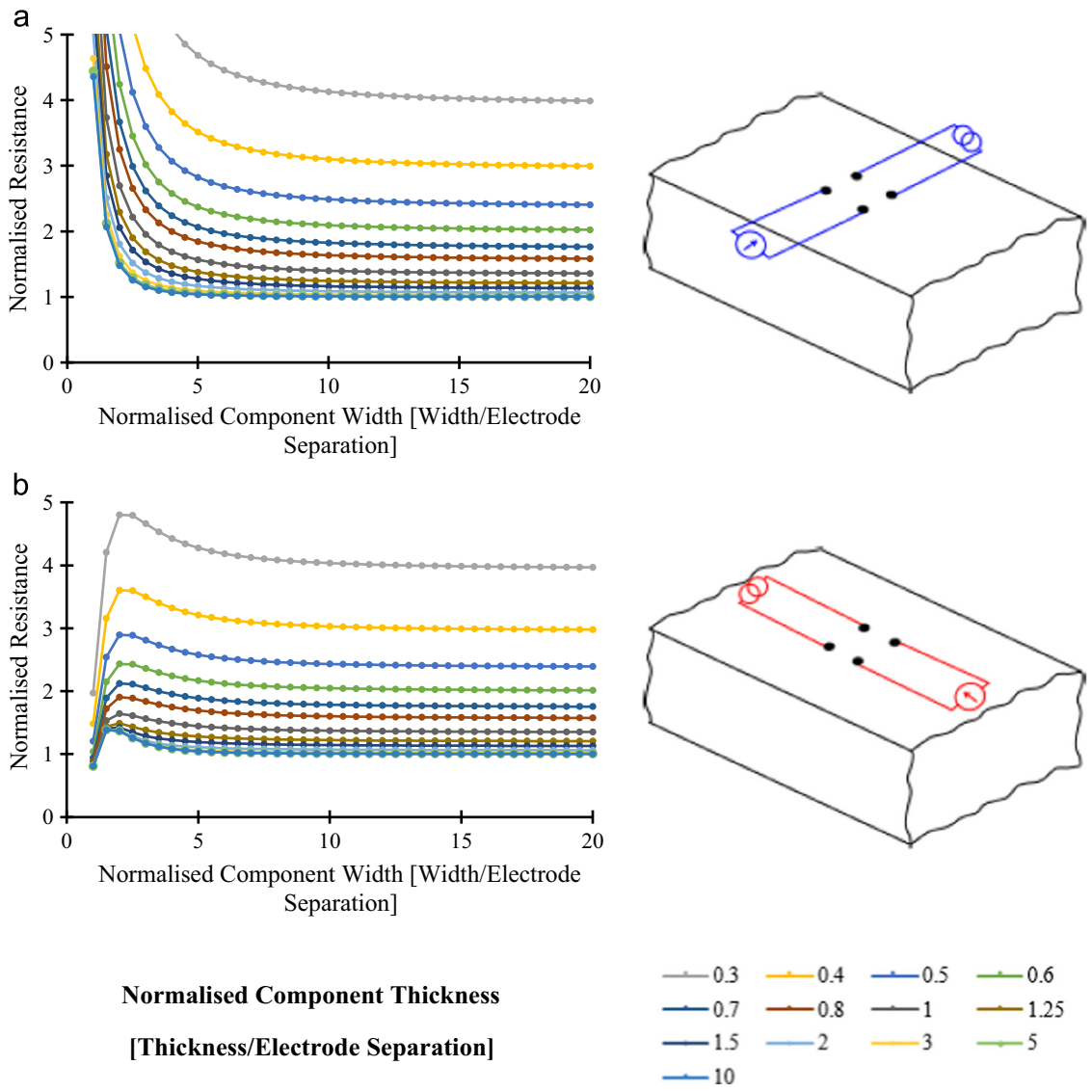

Fig. 3. The influence of finite component width and thickness on square arrangement transfer resistances. (a) Transfer resistances calculated with injection and sensing electrode pairs aligned normal to infinite component direction, as shown in schematic. (b) Transfer resistances calculated with injection and sensing electrode pairs aligned in infinite component direction, also shown in the corresponding schematic.

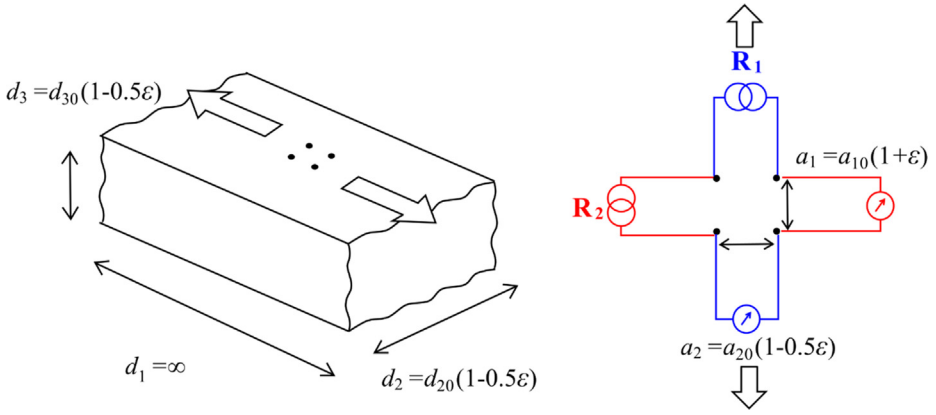

Fig. 4. Schematic showing the finite dimension component and how strain-like deformation can be added to the component and electrode configuration.

estimation of initial effective aspect ratio by resistance ratio relies on the assumption that the resistances are not influenced by edge effects. In the presence of edge effects compensation of imperfect electrode placement will be conceded as less accurate. It can be shown that the effect of a non-square initial geometry has no influence on the Normalised Resistance Ratio inversion but the

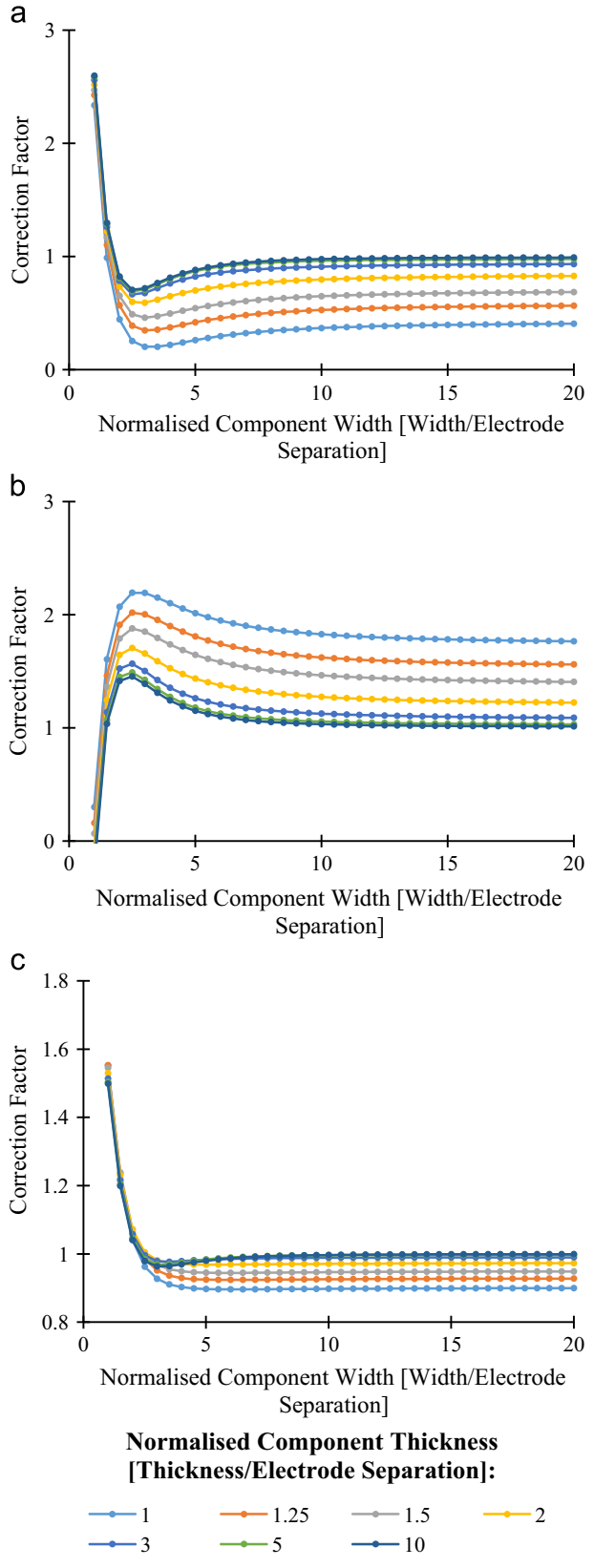

Fig. 5. Correction factors, k, for (a) the Normalised Resistance inversion for strain in the long component direction, (b) the Normalised Resistance inversion for strain in the short component direction and (c) the Normalised Resistance Ratio inversion. Strain values calculated from the inversion of potential drop data, $\varepsilon_{calculated}$, should be divided by the correction factor, so that $\varepsilon_{corrected} = \varepsilon_{calculated}/k$. Correction for normalised thicknesses of less than one and normalised widths of less than two should not be attempted, but are included for illustration.

Normalised Resistance inversion will produce orthogonal strain components where one is over estimated and the other is underestimated, depending on the initial electrode misplacement [31].

It is important to remember that it is only in slender components that imperfect electrode placement cannot be addressed in the inversion process, but it is also worth noting that slender components are almost always loaded uniaxially and therefore the Normalised Resistance Ratio inversion can be used. The issue is therefore included only for completeness. Finally, from a practical perspective, the larger the electrode separation the less influence a given electrode misplacement will have on the imperfect square geometry.

4. Experimental validation

In order to demonstrate the ability of the potential drop technique to successfully invert strain, two sets of experiments were conducted. The first experiment was on a large tensile test specimen designed to remove edge effects; it was plastically deformed at room temperature so that detailed independent strain measurements could easily be taken. Second, a series of accelerated creep tests was conducted to demonstrate the ability of strain inversion in creep conditions.

4.1. Room temperature tensile test component

A S275 mild steel tensile specimen with a gauge cross section of 75 mm × 24 mm and gauge length 150 mm was produced, as shown in Fig. 6. To one side of the specimen a random speckle pattern was painted for the purpose of taking an independent strain measurement using digital image correlation (DIC). On the reverse side of the specimen, a 1 × 10 element array of 5 mm electrode separation potential drop sensors was installed, similar to that shown in Fig. 2(a). The sample was tested using a 2.5 MN Instron tensile test machine. A Stanford Research SR830 Lock-in amplifier was used with a 1 Hz, 300 mA inspection current.

Each element of the PD array can be compared to the strain field as measured by DIC in the corresponding region on the reverse side of the component. A single Nikon D7000 digital camera with Nikkor 200 mm macro-lens was used giving 4928 × 3264 pixels. Out of plain movement is assumed to be zero. A stochastic speckle pattern was applied with acrylic spray paint to ensure good adhesion to the steel sample at large strains. An image is divided into facets which contain enough features (speckle pattern) to allow the position of those facets to be identified in subsequent images [39]. The images were processed using commercial DIC software Aramis [40].

The component was quasi-statically deformed with a constant displacement rate of 0.2 mm/h, equivalent to an initial strain rate of ~0.0013 /h. As this was a uniaxial stress test the component is expected to deform with constant volume, contracting with a strain of half that of the extension in the loading direction ($\varepsilon_{normal} = -0.5\varepsilon_{loading}$) prior to necking.

Fig. 7 compares the results of the potential drop measurements and the DIC strain measurements taken from the corresponding area on the reverse of the component. The left hand results of Fig. 7 show the result of the Normalised Resistance inversion while the right show the result of the Normalised Resistance Ratio inversion. All resistances normalised to the initial unloaded values. Only four of the 10 of the elements are shown for brevity.

Up until necking at about 130 h the two inversions are in very good agreement with each other and the DIC strain measurements. Following this point the assumption of uniaxial stress is locally violated, undermining the assumed strain ratio of $\varepsilon_{normal} = -0.5\varepsilon_{loading}$; this is seen in Fig. 7(e)–(h) to cause substantial error in the Normalised Resistance Ratio inversion in the central elements towards failure. It is

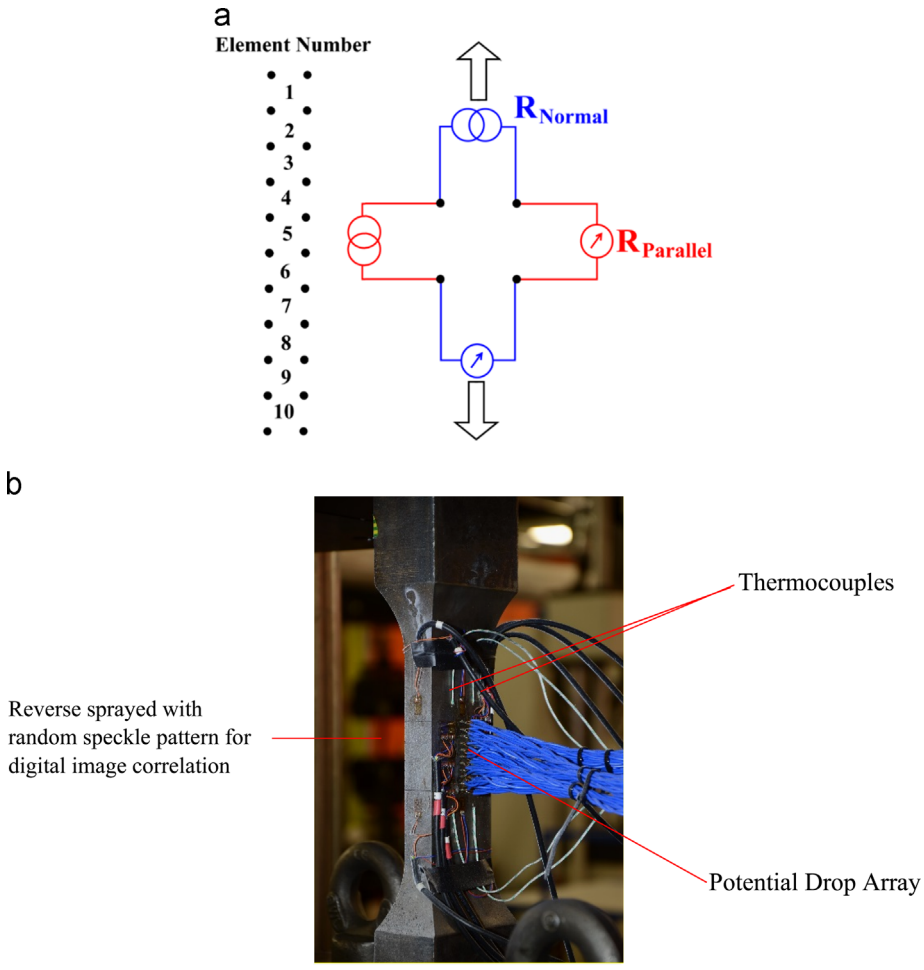

Fig. 6. (a) Schematic showing potential drop array measurement arrangement. Annotated photograph of room temperature tensile test specimen. The component cross section dimensions are 50 mm × 25 mm in the gauge length.

important to note the extreme strain that has accumulated by this stage and such problems are not expected in the creep of power station components. Excellent agreement can be seen between the Normalised Resistance inversion and the DIC measurement well beyond the initiation of necking as there is no required assumption about the stress state. The painted speckle pattern which provides the reference points for the DIC method eventually disintegrates and separates from the test component at large strains; this can be seen occurring towards failure in element 7. The good agreement between the Normalised resistance inversion and the potential drop results indicate that both techniques are working effectively up to large strains.

4.2. High temperature creep tests

Creep samples of 24 mm × 10 mm gauge cross section were produced and 1 × 8 element potential drop arrays with 5 mm electrode separation installed. This equates to normalised width of 4.8 and normalised thickness of 2. Three creep tests on virgin P91 material were conducted at 620 °C and stresses of 115 MPa, 130 MPa and 160 MPa. Results of all three tests are shown by Corcoran [31] but only the longest duration 115 MPa experiment will be shown in this paper. The elasticity modulus of P91 steel is approximately 165 GPa at 630 °C [41].

A motivation for the present work is the lack of technology to provide a robust, high temperature strain measurement. As a consequence the greatest difficulty in demonstrating the strain inversion was providing an independent strain measurement to verify the results obtained by PD. A number of technologies and techniques were attempted but were found to be prohibitively unreliable. An additional complication was that, due to the large stress and temperature dependence of creep, the strain along the gauge length of the uniaxial creep specimens was found to be non-uniform. The independent strain measurement would therefore have to match the gauge length of the PD measurement. A set of extensometry was produced that could be mounted to the rear of the creep specimen via M3 spot welded studs which would transfer the displacement outside of the furnace where it could be measured using a linear variable differential transformer (LVDT). The studs were initially separated to cover an integer number of PD elements (in this case four); in this way a larger gauge length could be used which is easier to implement. As each of the potential drop array elements was initially of the same size the engineering strain measured by extensometry should match the average engineering strain of the encompassed PD elements. In the schematic of Fig. 8 the studs used for mounting the extensometry cover the central 4 PD elements; the strain as measured by the LVDT, ε_{LVDT}, should match the average of the strain as measured by the PD elements 3–6, $\varepsilon_{PD3} - \varepsilon_{PD6}$.

Fig. 9 shows the result of the Normalised Resistance Ratio inversion for each of the elements of the potential drop array for the duration of the experiment. It can be observed that the strain rate is considerably higher in the central array elements than those towards the ends. This is due to the widening of the dog bone specimen influencing the stress state. Towards failure, further strain localisation is evident until failure finally occurs at

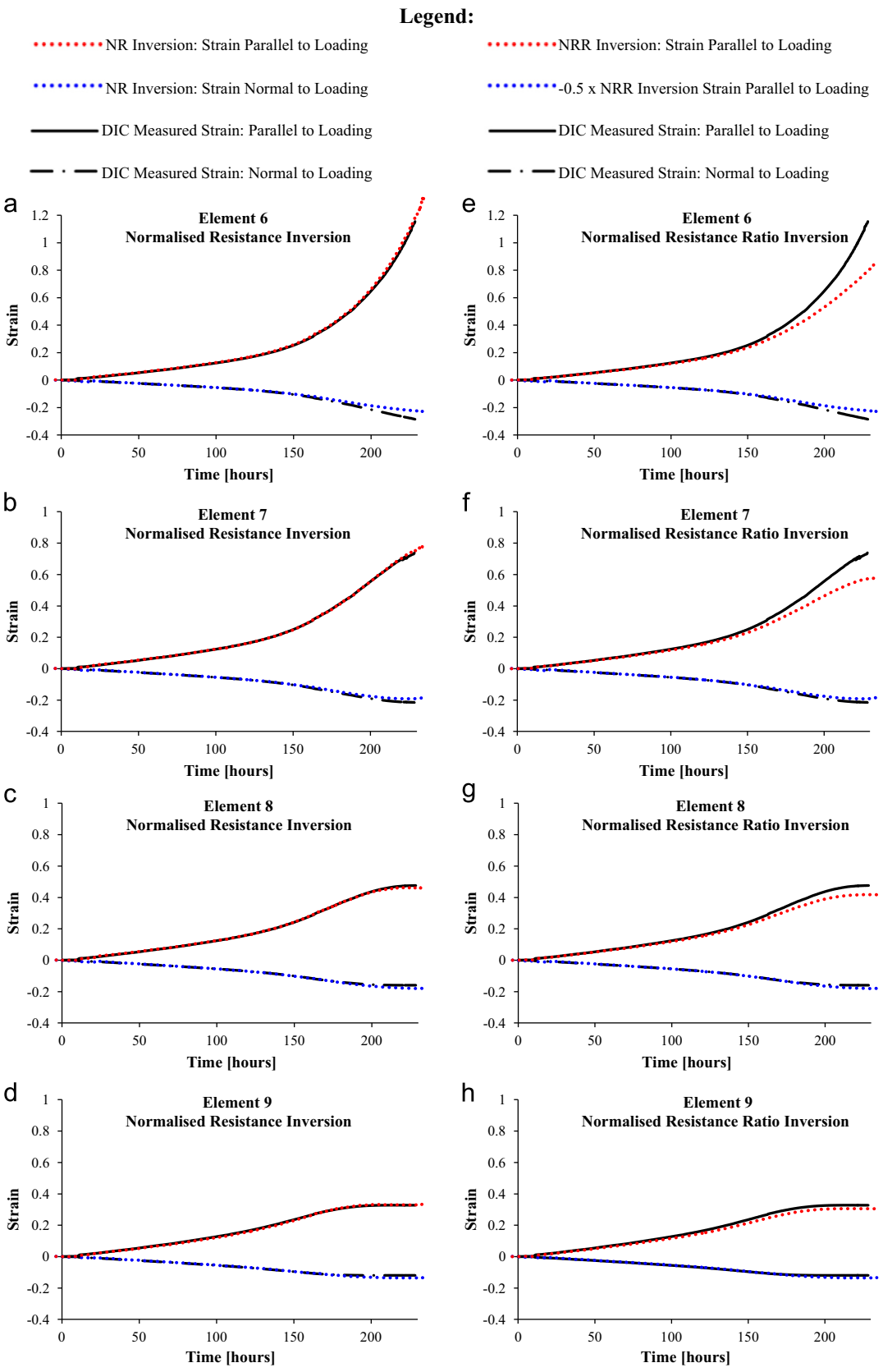

Fig. 7. Comparison between potential drop measured strain (red dashed lines) and DIC measured strain (black continuous lines). (a)–(d) On the left show the result of the Normalised Resistance inversion while (e)–(h) on the right show the result of the Normalised Resistance Ratio inversion for elements 6–9 of the array shown in Fig. 6(a). (For interpretation of the references to colour in this figure legend, the reader is referred to the web version of this article.)

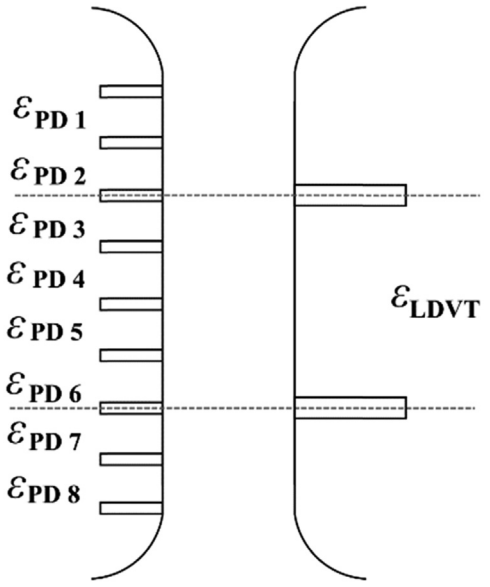

Fig. 8. Schematic showing side profile of a creep test component. On one side an array of potential drop sensors is installed while on the reverse studs have been mounted for strain to be measured by LVDT via extensometry.

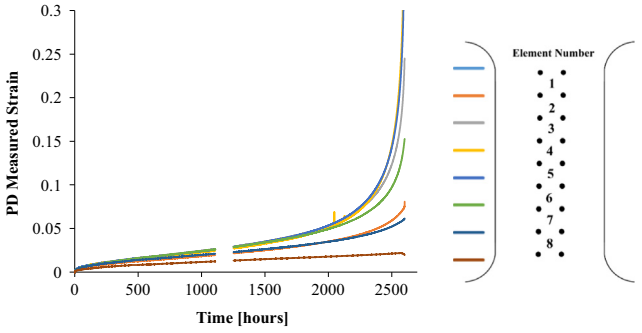

Fig. 9. Uniaxial Creep Test 3: P91, 620 °C, 115 MPa. Result of the Normalised Resistance Ratio strain inversion for each element of the potential drop array, with the exception of element 1 which failed prior to loading. The missing data is a result of a computer failure.

element 4. In this experiment a computer malfunction leads to the missing data following 1100 h. Element 1 of the array failed before loading started.

The studs used for mounting the extensometer covered only array elements 3–6 in this experiment, as illustrated in Fig. 8. The average strain from these elements is compared to the control extensometry results. To include in the comparison the strain component of the Normalised Resistance inversion normal to the loading direction it is multiplied by −2. The edge effects have been compensated using values taken from Fig. 5. The limited influence of electrode placement on the Normalised Resistance Ratio inversion means that agreement is very good. The slender geometry of the test component means that imperfect electrode placement cannot be properly accounted for and therefore the two Normalised Resistance inversion results straddle the extensometry readings; a familiar feature in such results.

Closer examination of Fig. 10 provides a useful insight into the behaviour of the inversions. There is a perturbation in the strain measurements between 450 and 600 h. This is caused by an air-conditioning failure in the laboratory causing a 12 °C increase under ambient conditions and a 1–1.5 °C decrease in furnace temperature. There is a slight change in the strain as measured by the LVDT through extensometry, presumably due to the temperature stability of the electronics. A similar effect is seen in the Normalised

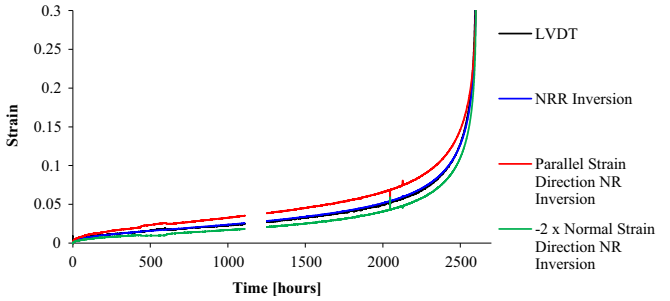

Fig. 10. Comparison of the strain measured by LVDT and the potential drop inversions. Central 4 elements of the potential drop array were averaged to match gauge length of the extensometer.

Resistance inversions; the inversion is resistivity dependent and therefore will be sensitive to changes in temperature. The Normalised Resistance Ratio however inherently suppresses resistivity changes and therefore is temperature insensitive.

5. Discussion

In order to inform evaluation of the two possible inversion options, the Normalised Resistance Ratio inversion and the Normalised Resistance inversion, a summary of attributes is provided in Table 1.

First, as evident from the results presented in this paper, accurate strain measurements can be accomplished using the proposed quasi-DC, square configuration, potential drop technique. In uniaxial accelerated creep tests the temperature is nominally constant and therefore reversible temperature dependent resistivity changes are not problematic. The effect of resistivity change from microstructural degradation does not appear to be noticeable, suggesting the influence on resistance is far smaller than the effect of strain. Inversion is possible using the Normalised Resistance Ratio inversion as the stress state must be uniaxial. Not only is the Normalised Resistance Ratio inversion preferable due to the suppression of resistivity changes but also has the feature that the influence of component edges and imperfect electrode positioning are minimal. It is therefore recommended that the Normalised Resistance Ratio be used for uniaxial laboratory tests on slender components. The technique offers the possibility to monitor local strain behaviour along the length of a component, providing enhanced information on component behaviour over extensometry techniques which inevitably average strain over a larger gauge length. This attribute may lend the technique to studies of weld behaviour where the different materials domains will have different strain responses. It should be emphasised, however, that this application is significantly different from the bulk material case described in this paper [23].

In uniaxial tests where significant strain localisation may occur, the assumption of uniaxial stress may be locally violated, as demonstrated in the large room temperature plastic deformation tests approaching failure. In this case the Normalised Resistance Inversion was necessary.

Although the temperature of a power station component is dictated by the boiler output at a nominal operation temperature, considerable temperature fluctuations are observed in practice [42]. Fortunately, the temperature dependence of resistivity is reversible and highly repeatable. Although it is not shown in this paper, temperature compensation can be implemented by the use of a temperature sensor in the vicinity of the measurement point. The irreversible resistivity change resulting from long-term microstructural degradation is expected to be much smaller than the effect of temperature but compensation will not be straight

Table 1
Summary of attributes of the Normalised Resistance Ratio and Normalised Resistance inversions.

Attribute	Normalised Resistance Ratio inversion	Normalised Resistance inversion
Resistivity dependent	Not sensitive to isotropic resistivity change or instrument gain change.	Yes
Requires information on stress state (informing $\varepsilon_1/\varepsilon_2$ ratio) in order to complete inversion	Yes – but will still provide information on aspect ratio. Sensitivity will be limited in cases approaching an 'equi-biaxial' stress state where the strain aspect ratio will not change.	No
Sensitive to component edges	Yes – but much less than the Normalised Resistance inversion. A normalised width of 5 with a normalised component thickness of 2.5 limits the correction factor to 0.98.	Yes – a normalised width of 5 with a normalised component thickness of 2.5 results in a correction factor of 0.78 for comparison.
Sensitive to imperfect electrode placement	No	Only when combined with edge effects

forward [31,43]. 'Dummy gauges' may be installed on sample material which is in good contact with the component under test, thereby being thermally but not mechanically coupled to a component. The dummy gauge will provide a measurement independent of strain indicating the expected resistivity change, offering a means to compensate for resistivity.

The significance of resistivity 'drift' on the accuracy of the inversion will depend on the magnitude of its influence on resistance compared to the influence of strain. In accelerated creep tests the time scale available for resistivity drift is small and strain in excess of 30% is produced; the relative influence of resistivity drift is therefore seen to be negligible. Clearly, the strain rate in the power station environment will be orders of magnitude lower than in the accelerated tests demonstrated here. Although direct measurements are rarely found in literature, design requirements limit the expected strain rate of components to be less than 1% per 100,000 h [44,45]. Even small resistivity changes could cause a significant error in strain rate calculations, therefore the use of the resistivity independent Normalised Resistance Ratio inversion is advised.

The result of the Normalised Resistance Ratio inversion is a strain, or aspect, ratio. An important limitation of the Normalised Resistance Ratio inversion is the decreasing sensitivity in cases approaching 'equi-biaxial' stress states; where the hoop and axial stress are equal. In such cases the ratio of orthogonal surface strains will be unity and therefore the aspect ratio of the electrode geometry will not change, despite the square increasing or decreasing in size. In power station pipe work a typical stress ratio between the orthogonal hoop and axial directions is 2:1, assuming a close-ended cylinder. Additional axial stress will result from the bending stress from the weight of the thick-walled component. It is however expected that the hoop stress will in general be greater than the axial stress [31]. Examination of the resistances directly or the Normalised Resistance inversion may help determine whether an 'equi-biaxial' stress state may be present and qualify whether the use of the Normalised Resistance Ratio inversion is permissible. Alternatively, periphery information, for example sensors at the same axial location but at different points around the circumference may be used to inform stress state.

In order to interpret this as strain the relationship between orthogonal strain components must be known. In power station components the stress state is unlikely to be known with reasonable certainty. The combination of hoop stresses from internal pressure and axial stresses arising from both internal pressure and significant bending stresses from the weight of the pipes results in a complex and situation specific stress state. Under these multiaxial conditions strain inversion based on the Normalised Resistance Ratio is not possible. It is worth noting, however, that the aspect ratio may still provide sufficient information on component integrity. As discussed in Section 1, it is the *increase in strain rate* that provides valuable component integrity information; it is proposed that the *increase in rate of change of aspect ratio* may be interpreted to infer damage state.

6. Conclusions

A strain sensitive potential drop technique has been presented. The technique is well-suited to high temperature or harsh environments where other sensors may not withstand the conditions. The use of quasi-DC frequencies suppresses the skin effect which would otherwise cause spurious resistance changes due to fluctuations in magnetic permeability, whilst offering improved noise performance over true DC measurements. The result is a low power measurement technique where measurements of around 100 mA are typical.

Two alternative inversion approaches have been proposed. The Normalised Resistance Ratio inversion benefits from the suppression of resistivity changes and is additionally less sensitive to edge effects and imperfect electrode positioning. The Normalised Resistance Ratio, however, is only sensitive to aspect ratio and therefore requires prior knowledge of the stress state in order to invert strain. In order to invert biaxial strain information the Normalised Resistance inversion is necessary, though this is vulnerable to changes in resistivity or even gain drift.

Two experiments were carried out to validate and demonstrate the strain inversion. First a room temperature plastic deformation test was conducted; a large component was used to remove edge effects and the ambient temperature permitted independent control strain measurements. A smaller geometry creep test was also conducted to show performance at high-temperature. Both experiments demonstrated good agreement with independent measurements.

The strain behaviour of power station components will be quite different from those exhibited by the accelerated uniaxial creep test shown in this paper. The resistivity dependence of the Normalised Resistance inversion, when combined with the extremely low strain rates expected in power station components, may undermine the success of the inversion in that context. Unfortunately, the stress state at a given location on a power station component is also unlikely to be known; this prohibits the use of the resistivity independent Normalised Resistance Ratio for strain inversion. Instead, it is proposed that the *rate of change of aspect ratio* is used as an indirect metric for strain rate that will allow a robust, low-power, continuous indication of component creep integrity and remnant life.

References

[1] Viswanathan R, Stringer J. Failure mechanisms of high temperature components in power plants. J Eng Mater Technol 2000;122:246. http://dx.doi.org/10.1115/1.482794.
[2] Viswanathan R. Life management of high-temperature piping and tubing in fossil power plants. J Press Vessel Technol 2000;122:305. http://dx.doi.org/10.1115/1.556187.
[3] Webster G, Ainsworth RA. High temperature component life assessment. London: Springer Science & Business Media; 1994.
[4] Dyson B. Use of CDM in materials modeling and component creep life prediction. J Press Vessel Technol 2000;122:281. http://dx.doi.org/10.1115/1.556185.

[5] Furtado HC, Le May I. High temperature degradation in power plants and refineries. Mater Res 2004;7:103–10. http://dx.doi.org/10.1590/S1516-14392004000100015.
[6] Sposito G, Ward C, Cawley P, Nagy PB, Scruby C. A review of non-destructive techniques for the detection of creep damage in power plant steels. NDT E Int 2010;43:555–67. http://dx.doi.org/10.1016/j.ndteint.2010.05.012.
[7] Le May I, Furtado HC. Creep damage assessment and remaining life evaluation. Int J Fract 1999;97:125–35.
[8] Penny RK. The use of damage concepts in component life assessment. Int J Press Vessel Pip 1996;66:263–80. http://dx.doi.org/10.1016/0308-0161(95)00101-8.
[9] Evans RW, Wilshire B. Introduction to creep. London: Institute of Materials; 1993.
[10] Penny RK, Marriott DL. Design for Creep. USA: Springer Science & Business Media; 1995.
[11] Cane BJ, Williams JA. Remaining life prediction of high temperature materials. Int Mater Rev 1987;32(1):241–64. http://dx.doi.org/10.1179/imr.1987.32.1.241.
[12] Ghia S, Certo M, De Michelis C, Rizzi L. On-line monitoring and non destructive techniques for measurement of creep deformation. In: Bicego A, Nitta A, Viswanathan R, editors. Materials ageing and component life extension; 1995.
[13] Allwood FP, Wilson JD. Creep strain management of power plant components. In: Chau FS, Lim CT, editors. Proceedings of international conference on experimental mechanics: advances and applications. International Society for Optics and Photonics; 1997. p. 238–43. doi:10.1117/12.269823.
[14] Maharaj C, Dear JP, Morris A. A review of methods to estimate creep damage in low-alloy steel power station steam pipes. Strain 2009;45:316–31. http://dx.doi.org/10.1111/j.1475-1305.2008.00465.x.
[15] Fortmann MD-I. Vorrichtung zur Dehnungsmessung; 1983. EP19830101654.
[16] Fidler R. The calibration of CERL-Planer capacitance strain gauges. Strain 1986;22:171–7. http://dx.doi.org/10.1111/j.1475-1305.1986.tb01872.x.
[17] Baumann B, Schulz M. Long-time high-temperature strain gauge measurements on pipes and dissimilar welds for residual lifetime evaluation. Nucl Eng Des 1991;130:383–8. http://dx.doi.org/10.1016/0029-5493(91)90230-F.
[18] Hoffmann K. An introduction to stress analysis and transducer design using strain gauges. 1987.
[19] van Zyl FH, von dem Bongart G, Bezuidenhout MEJ, Doubell P, Havinga FC, Pegler DAH, et al. Life assessment and creep damage monitoring of high temperature pressure components in South Africa's power plant. In: Proceedings of ECCC Creep Conference; 2005. p. 934–45.
[20] Nagy PB. Electromagnetic nondestructive evaluation. In: Kundu T, editor. Ultrasonic and electromagnetic NDE for structure and material characterization: engineering and biomedical applications. Boca Raton, USA: CRC Press; 2012. p. 890.
[21] McMaster RC. Electric current test principles. Nondestructive testing handbook. 1st ed. New York: Ronald Press; 1959. p. 35.1–11.
[22] Sposito G. Advances in potential drop techniques for non-destructive testing [Ph.D. thesis]. Imperial College London; 2009.
[23] Corcoran J, Nagy PB, Cawley P. Potential drop monitoring of creep damage at a weld. In: Chimenti DE, Bond LJ, Thompson DO, editors. Review of progress in quantitative nondestructive evaluation. AIP Publishing. vol. 170002; 2016. http://dx.doi.org/10.1063/1.4940625.
[24] Corcoran J, Davies CM, Nagy PB, Cawley P. Potential drop strain sensor for creep monitoring. In: Proceedings ASME 2014 pressure vessels & piping conference. Anaheim, California, California: ASME; 2014.
[25] Byeon JW, Kwun SI. Nondestructive evaluation of thermally degraded 2.25Cr – 1Mo steel by electrical resistivity measurement. Mater Trans 2003;44:1204–8.
[26] Seok C-S, Bae B-K, Koo J-M. DC potential drop method for evaluating material degradation. KSME Int J 2004;18:1368–74.
[27] Yu KM, Nahm SH, Kim YI. Toughness degradation evaluation of 1Cr–1Mo–0.25V steel by electrical resistivity. 8; 1999. p. 1175–6.
[28] Pelloux RM, Peltier JM, Zilberstein V A. Creep testing of 2.25 Cr-1 Mo welds by DC potential drop technique. J Eng Mater Technol 1989;111(19). http://dx.doi.org/10.1115/1.3226426.
[29] Vasatis IP, Pelloux RM. Application of the dc potential drop technique in investigating crack initiation and propagation under sustained load in notched rupture tests. Metall Trans A 1988;19:863–71. http://dx.doi.org/10.1007/BF02628369.
[30] Vasatis IP. The creep rupture of notched bars of IN-X750 [Ph.D. thesis]. Massachusetts Institute of Technology; 1986.
[31] Corcoran J. Creep monitoring using permanently installed potential drop sensors [Ph.D. thesis]. Imperial College London; 2015. ⟨https://workspace.imperial.ac.uk/nde/Public/Corcoran-J-2015-Thesis%20(002).pdf⟩.
[32] Voss RF. 1/f (Flicker) noise: a brief review. In: Proceedings of the 33rd annual symposium on frequency control; 1979. p. 40–6. ⟨https://dx.doi.org/10.1109/FREQ.1979.200297⟩.
[33] Madhi E, Nagy PB. Sensitivity analysis of a directional potential drop sensor for creep monitoring. NDT E Int 2011;44:708–17. http://dx.doi.org/10.1016/j.ndteint.2011.08.001.
[34] Corcoran J, Cawley P, Nagy PB. A potential drop strain sensor for in-situ power station creep monitoring. AIP Conf Proc 2014;1581(33):1482–7. http://dx.doi.org/10.1063/1.4864997.
[35] Jiles DC. Introduction to magnetism and magnetic materials. 2nd ed.. Boca Raton, USA: CRC Press; 1998.
[36] Matelect Ltd. AC or DC, A Primer for Decision Makers 2015.
[37] Naumenko K, Altenbach H. Modeling of creep for structural analysis. Berlin Heidelberg: Springer; http://dx.doi.org/10.1007/978-3-540-70839-1.
[38] Lu Y, Bowler N, Bowler JR, Huang Y. Edge effects in four-point direct current potential drop measurements on metal plates. J Phys D: Appl Phys 2009;42:135004. http://dx.doi.org/10.1088/0022-3727/42/13/135004.
[39] Sutton MA, Orteu JJ, Schreier H. Image correlation for shape, motion and deformation measurements: basic concepts, theory and applications. Springer Science & Business Media; 2009.
[40] Aramis, GOM; http://www.gom.com/3d-software/aramis-software.html, 2012.
[41] Haarmann K, Vaillant JC, Vandenberghe B, Bendick W, Arbab A. The P91/T91 Book. Boulogne: Vallourec and Mannesmann Tubes; 2002.
[42] Morris A. Personal communication; 2015.
[43] Pollock DD. Physical properties of materials for engineers. Boca Raton, USA: CRC Press; 1993.
[44] EPRI. Fossil plant high-energy piping damage: theory and practice. Piping fundamentals. Vol. 1; 2007.
[45] Viswanathan R. Damage mechanisms and life assessment of high temperature components. USA: ASM International; 1989.